Made available through Montana State University's ScholarWorks

Dichroic Mueller pulsed lidar testbed

Nathaniel J. Field and Joseph A. Shaw

Accessibility Disclaimer:

For a more accessible version of this document, please submit an accessibility request form through the Montana State University Library website.

OE Optical Engineering

RESEARCH PAPER

Dichroic Mueller pulsed lidar testbed

Nathaniel J. Field and Joseph A. Shaw*
Montana State University, Electrical and Computer Engineering, Bozeman, Montana, United States

ABSTRACT. We describe the design and implementation of a dichroic Mueller pulsed lidar (DMPL) testbed. Operating at 532- and 1064-nm wavelengths simultaneously, the polarimetric lidar returns a full set of range-resolved Mueller matrix coefficients after a measurement period of just under 3 min. The instrument is designed as a source of reference measurements to produce proof-of-concept and high-fidelity scene models for the validation of a wide variety of other, more complex polarimetric lidar systems. Using polarimetric optimization theory and assessing the limits of our alignment and calibration, we bounded the theoretical Mueller coefficient errors to no more than 2.04%. Initial measurements show expected polarimetric features for samples characterized in the existing literature and a vast majority of measured coefficients well within the theoretical maximum error; the mean observed Mueller coefficient error across multiple scenarios was 0.86%.

© The Authors. Published by SPIE under a Creative Commons Attribution 4.0 International License. Distribution or reproduction of this work in whole or in part requires full attribution of the original publication, including its DOI. [DOI: 10.1117/1.OE.64.7.074103]

Keywords: polarimetry; lidar; Mueller; polarization

Paper 20250276G received Apr. 4, 2025; revised Jun. 16, 2025; accepted Jun. 17, 2025; published Jul. 7, 2025.

1 Introduction

Lidar remote sensing can often benefit from the use of optical polarization to gain additional information about the scene being probed. For example, early atmospheric lidar researchers found that measuring backscattered light in the transmitted state (co-polarized) and an orthogonal state (cross-polarized) enabled reliable discrimination of the cloud thermodynamic phase.[1–4] Although the expansive study by Houston and Carswell showed that dual-polarization lidar was sufficient for most forms of atmospheric or oceanographic polarized lidar applications,[5] there was still room for basic research on polarized ladar (lidar that focuses on ranging more opaque samples rather than scattering media). Although some studies have sought optimal transmit and receive states for specific detection scenarios,[6] others have applied the simple dual-polarization method as an initial option and found results that were improved sufficiently to deem the complexity of full Mueller polarimetric lidar unnecessary.[7–9] The prevalence of dual-polarization lidar led to the formalization of its operating theory in 2008[10] and an extension to complete polarimetric lidar theory derived from Stokes vectors and Mueller matrices 4 years later.[11] However, there remains interest in fully polarimetric lidar for applications not yet fully studied, such as a full-polarimetric lidar for detecting chiral biological warfare agents[12,13] or a single-pulse polarimetric lidar developed by the Air Force Research Lab.[14–17] Such applications show that there is still significant room to explore optimal transmit and receive states for various phenomenology studies and object detection-and-classification scenarios,[16] and fundamental research instruments with well-quantified tolerance can help provide information to support theories and assumptions used by these more complex instruments.

*Address all correspondence to Joseph A. Shaw, joseph.shaw@montana.edu

Polarimeter optimization theory is based largely on passive polarimetry[18–23] but extends naturally to active polarimetry as well.[24,25] These existing theories can be applied to the selection of optimal polarization states used by a receiver (polarization state analyzer, PSA) or a transmitter (polarization state generator, PSG) for active systems. The theories present the condition number as a relatively simple method of propagating error and uncertainty in a receiver or transmitter to the final Stokes or Mueller coefficients. Despite frequent use and reference to these optimal state theories in the literature, relatively few studies used optimization metrics such as the condition number to bound expected uncertainties and, to our knowledge, this is limited to modeled systems.[26,27]

When designing and building polarimeters for specific applications, there is frequent use of the optimization theories discussed above. However, there is a lack of applications that use these theories for error propagation that bounds the uncertainties expected in the Stokes parameters or Mueller matrix coefficients, especially from active polarimeter systems. It is more common for these systems to be used to measure a quality polarization element, such as a linear polarization filter (LP) or quarter-wave retarder (QWP), and report their measured Mueller matrix compared with that expected for the validation element.[14,28,29] Although validation is an important step in quantifying uncertainty, the use of well-constrained standards such as LPs and QWPs can reduce the impact of error propagation through multiple terms and may miss error propagation in elliptical Mueller coefficients ($m_{_3}$ or $m_{3_}$). However, combining validation with calculations using the condition number and dominant uncertainties in a transmitter and receiver provides a more robust tolerance on measurements made by a polarimetric instrument. Some literature has addressed these issues and proposes the use of the eigenvalue calibration method[30,31] to capture all the uncertainties in a PSA or PSG without creating a model; however, this method requires uncertainties in these modulators to not change between measurements, which is not well suited to division-of-time systems with rotating polarization elements.

In this work, we address these gaps by describing a simple Mueller polarimetric lidar that can measure the range-dependent Mueller matrix of objects in a scene with coefficient uncertainties bounded by error propagation with the well-established polarimeter optimization theories previously cited. The lidar transmitter is a PSG based on the well-established dual-rotating-retarder design, and the lidar receiver is a functionally similar PSA. The separate designs of the pulsed lidar and the PSG and PSA are built on well-established fundamentals, and we believe this is the first instance of a ranging active polarimeter that applies both maximum uncertainty bounds calculated from polarimeter optimization theory and validation measurements. This particular instrument was designed and built to leverage its bounded uncertainty to produce science-grade Mueller matrix measurements of materials under a wide range of application scenarios. In this way, this instrument serves as a validation testbed for the other instruments, which have demonstrated interest in full-polarimetric lidar/ladar applications.

2 System Design

The dichroic Mueller pulsed lidar (DMPL) aims to provide a relatively simple system to measure polarimetric responses of sample materials and scenes with well-characterized polarimetric accuracy and precision. We explain the fundamental instrument design, the assessment of theoretical polarimetric accuracy, the limitations of measurement rates with high precision, and considerations for testing at variable range windows. A labeled overhead view of the DMPL transmitter and receiver is shown in Fig. 1.

2.1 Key Components

The fundamental instrument builds on a previously developed nonranging polarimeter,[32,33] adding a pulsed laser transmitter, avalanche photodiodes (APDs) receivers, a high-speed analog-digital converter for signal acquisition, and a high-speed photodiode as an optical trigger. The transmitter is an ND:YAG pulsed laser (Quantel Ultra) operating simultaneously at 532- and 1064-nm wavelengths, with 6.86 ns pulse width (full-width at half-max), 34.6 mJ pulse energy at 532 nm, and 14.6 mJ pulse energy at 1064 nm.

The transmitter includes a 10× beam expander that has been slightly defocused such that the output beam is ~40 mm in diameter with 5-mrad divergence. Basic visual inspection suggests

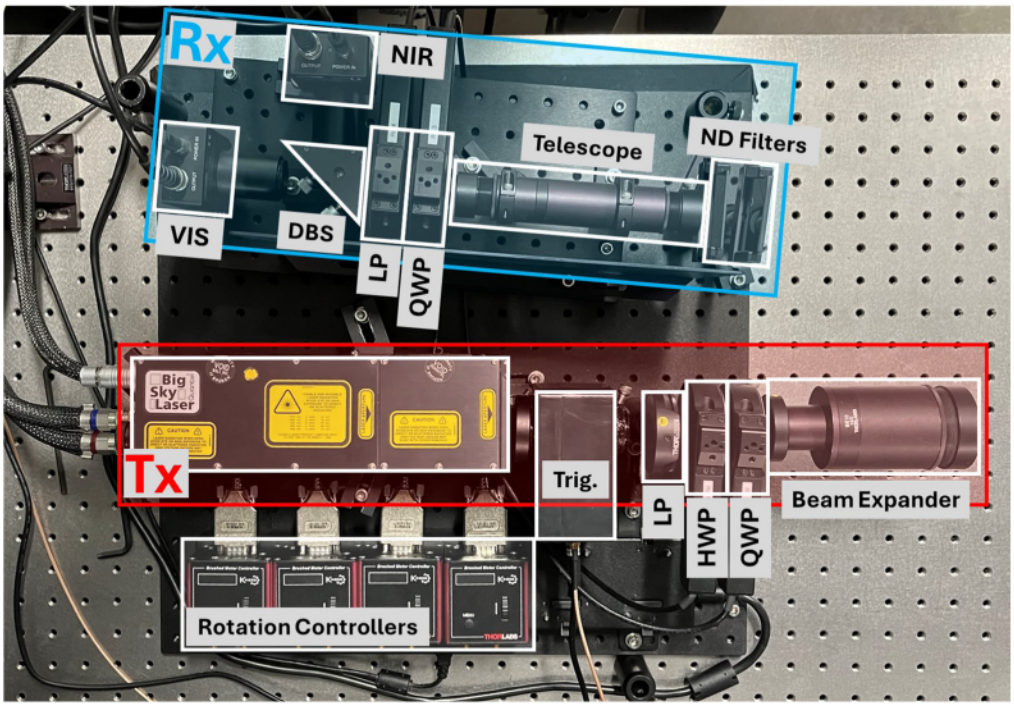


Fig. 1 DMPL transmitter (red) and receiver (blue), mounted on an optical breadboard. This assembly weighs about 16 kg, sufficiently light and rigid to be mounted on a motorized pan-tilt mount with a full range of motion.

the beam is primarily in the TEM00 mode, but the entire illuminated area is within the single-pixel receiver field of view (FOV) when calibrated measurements are necessary, so an exact M^2 value was not calculated as it was not necessary. The receiver telescope is made up of two plano-convex lenses set for 0.5× magnification and defocused slightly such that collimated light on the detector side has a 15-mrad divergence on the scene side of the telescope. The focusing lenses in front of the detectors are aligned such that collimated light should fall directly on the active area, setting the field rays.

The receiver splits the spectral channels using a dichroic beam splitter (DBS), using a Si APD (ThorLabs APD430A, Newton, New Jersey, United States) to collect the 532-nm channel and an InGaAs APD (ThorLabs APD430C) to collect the 1064-nm channel, both of which are specified to have electrical bandwidths up to 400 MHz (rise time of 0.875 ns). The digitizer is a GaGe CSE161G2 with a 1 GS/s sample rate, 16-bit resolution, and 600 MHz electrical bandwidth. The digitizer is externally triggered, and we implemented an optical trigger in the form of a high-speed photodiode (ThorLabs DET025A) viewing side-scattering from the transmitter.

The polarization elements are split into a polarization state generator (PSG) in the transmitter (Tx) and a polarization state analyzer (PSA) in the receiver (Rx). The PSG begins with an LP aligned to the laser output major polarization axis, cleaning up the initial linear state with maximum power throughput. After the clean-up polarizer, a rotating half-wave retarder (HWP) rotates the orientation of the linear polarization state without variable attenuation, and a QWP can be rotated relative to the HWP to produce any ellipticity in the output polarization state. The PSA consists of a QWP followed by an LP to attenuate signals based on their incident polarization, both in terms of ellipticity and major polarization axis orientation. The HWP is a Meadowlark SAHM-100-420/1100, the QWPs in both the PSG and PSA are Meadowlark DQQ-100-532/1064, and the LPs in both the PSG and PSA are Meadowlark VFR-100-NIR; due to their matching specifications, discussion of either LP or QWP is relevant to both the transmitter and receiver. Each of these elements is mounted in a motorized rotation stage (ThorLabs PRM1Z8) with inter-measurement repeatability of 0.3 deg (0.1 deg for a set of measurements, and 0.2 deg when the motors are power cycled and homed again). These motorized stages account for hysteresis in their reported bidirectional repeatability, but we have programmed the stages to always approach a given angle from the same direction for improved accuracy.

2.2 Polarimetric Accuracy

Assuming reasonable quality polarizers and retarders, optimizing polarimetry relies mainly on the proper selection of PSG and PSA states. Previous literature showed that the optimal PSG states in an active system are matched to the optimal PSA states.[30,34] Optimal PSA states occur when each of the states is of equal similarity to each of the other states.[20,21] This is most easily conceptualized as optimization occurring when the coordinates for the PSA states on the Poincaré sphere form the vertices of a platonic solid (tetrahedron, cube, octahedron, dodecahedron, or icosahedron). Because there are only five platonic solids, there are only five possible optimal numbers of measurements for full-polarimetric measurement: four measurements (tetrahedron), six measurements (octahedron), eight measurements (cube), twelve measurements (icosahedron), or twenty measurements (dodecahedron). For simplicity, our original selection consisted of four states, starting with right-hand circular polarization, with Poincaré coordinates ($2\theta_{PF}$, 2ε, I_P) of (0 deg, 90 deg, 1), and three additional semi-elliptical states at (0 deg, −19.4712 deg, 1), (120 deg, −19.4712 deg, 1), and (−120 deg, −19.4712 deg, 1); θ_{PF} is the orientation of the polarization trace's major axis, and ε is the ellipticity of the polarization. However, as the high angular dependence of retarders is one of the largest potential sources of polarimetric error, it is best to minimize the total retardance required to generate or analyze the four states. This results in a rotation to two purely linear states—(125.2644 deg, 0 deg, 1) and (−125.2644 deg, 0 deg, 1)—and two elliptical states with reversed rotation directions—(0 deg, 54.7356 deg, 1) and (0 deg, −54.7356 deg, 1). The Poincare coordinates of the initial and rotated optimal coordinates are shown in Fig. 2.

One common metric used to describe polarimetric resolution is the condition number, κ, of the analysis matrix, $\mathbf{W}$; well-established in the field,[35] and particularly well-explained by Sabatke[20] and Tyo.[19,21,24] The analysis matrix, $\mathbf{W}$, is a well-established method of measurement demodulation in polarimetry with standard methods of generation for a PSA, PSG, or combination of the two (we follow the methods and theory laid out in section 7.4 of Chipman et al.'s textbook[35]). The condition number represents the maximum error propagation from the measurements to the calculated polarization values, either the Stokes vector values for passive polarimetry or the Mueller matrix coefficients for active polarimetry. The analysis matrix is derived from the Mueller matrices describing the PSA states or PSG states as

$$\mathbf{W} = \begin{bmatrix} \mathbf{M_0^1} \\ \mathbf{M_0^2} \\ \mathbf{M_0^3} \\ \mathbf{M_0^4} \end{bmatrix} = \begin{bmatrix} m_{00}^1 & m_{01}^1 & m_{02}^1 & m_{03}^1 \\ m_{00}^2 & m_{01}^2 & m_{02}^2 & m_{03}^2 \\ m_{00}^3 & m_{01}^3 & m_{02}^3 & m_{03}^3 \\ m_{00}^4 & m_{01}^4 & m_{02}^4 & m_{03}^4 \end{bmatrix}, \tag{1}$$

where M_0^i is the first row of the matrix for the i'th state. The condition number is then calculated as

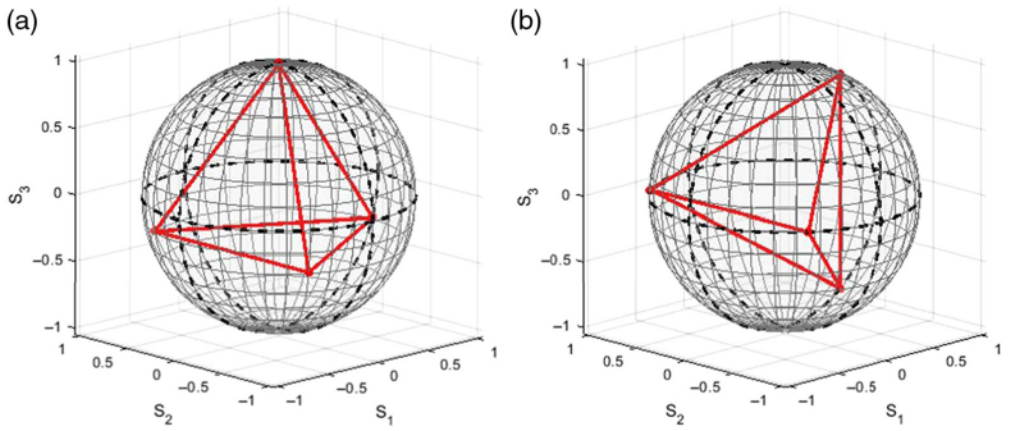


Fig. 2 Poincarè sphere coordinates for the initial optimal tetrahedron (a) and the tilted tetrahedron (b), which accounts for minimizing ellipticity.

$$\kappa(\mathbf{W}) = \|\mathbf{W}\|_2 \|\mathbf{W}^{-1}\|_2 = \frac{\sigma_{\max}(\mathbf{W})}{\sigma_{\min}(\mathbf{W})}, \tag{2}$$

where $\|\cdot\|_2$ is the L^2 norm and $\sigma_{\max}$ and $\sigma_{\min}$ are the maximum and minimum singular values decomposition. In the case that $\mathbf{W}$ is singular (or near-singular), it may be necessary to calculate κ using the pseudo-inverse rather than the inverse. Even for optimal configurations, κ still has a minimum value greater than 1; the minimum for linear polarimetry is $\sqrt{2}$, whereas the minimum for full polarimetry (including elliptical states) is $\sqrt{3}$.[19–21,24] Equation (2) assumes that $\mathbf{W}$ is invertible, or that we can at least get a pseudo-inverse; this is a safe assumption for the analysis matrix when using near-optimal states and with a rank that allows for complete solutions (minimum rank 4 for Stokes polarimetry or rank 16 for Mueller polarimetry).[35]

Although PSG and PSA states are chosen precisely, the reality of polarization filters, retarders, and their mounts introduce potential error. Each polarization element has associated tolerances for its effects on incident light. We can apply these tolerance values as maximum deviations from the expected PSG and PSA Mueller matrices, producing a new κ for the $\mathbf{W}$ matrix for each combination of positive or negative deviations; the worst-case scenario value for κ is then our accepted system value.

For an LP, we should consider the extinction ratio, r_e, and the tolerance on the major axis orientation angle, $\Delta\theta_p$. For a QWP or HWP, we should consider the retardance tolerance, $\Delta\phi_\Delta$, and the tolerance on the crystal axis orientation angle, $\Delta\theta_f$. For the LPs used, r_e is about 1100 at 532 nm and 3800 at 1064 nm. For the HWP, $\Delta\phi_\Delta$ is about $\lambda/200$ for both wavelengths, and for the QWPs, it is a maximum of $\lambda/100$ for both wavelengths. The clean-up polarizer is at a fixed angle that defines the polarization coordinate system of the device (and therefore does not contribute to polarimetric error other than a global orientation offset), whereas the remaining components are mounted in rotation stages with a maximum intra-measurement-set $\Delta\theta$ equal to 0.1 deg. The uncertainty values from the rotation stage spec sheet were not validated in the lab because any attempt to fit sinusoids to rotating polarizers with Malus' Law would have measurement uncertainties (from SNR and any reference polarizer angular uncertainty) that surpass the specified rotational uncertainty.

Applying these tolerance values while generating $\mathbf{W}$, the worst-case scenario condition numbers were $\kappa_{532,G} = 1.7792$, $\kappa_{532,A} = 1.7932$, $\kappa_{1064,G} = 1.7769$, and $\kappa_{1064,A} = 1.7908$ (for the 532-nm channel generator and analyzer and the 1064-nm channel generator and analyzer, respectively). On average, this represents a combined maximum propagating magnification of uncertainty of 3.19 for the 532-nm channel and 3.18 for the 1064-nm channel, which are both ~1.06× higher than the best case scenario of 3× magnification, respectively.

The dominant source of error in the transmitter arm is the pulse energy tolerance and the dominant source of error in the receiver when used with the majority of the APD dynamic range is the integrated noise. The pulse energy is specified as stable to within 0.61% when operating at 95% power (as we do in our measurements); scaling by $\kappa_{532,G}$ and $\kappa_{1064,G}$, respectively, this contributes 1.09% and 1.08% error to the Mueller coefficients via the generator arm for the respective channels.

The potential coefficient error from the receiver is more dependent on the amount of dynamic range used and, therefore, the maximum measurement value. However, we can make a very conservative constraint that we will be operating with a maximum signal not less than one-tenth of the dynamic range (170 mV). The APDs have specified RMS noise of 0.46 mV for the 532-nm channel and 1.02 mV for the 1064-nm channel. Scaling by the condition numbers $\kappa_{532,A}$ and $\kappa_{1064,A}$ for error propagation, we can therefore expect not more than 0.48% (532-nm) or 1.07% (1064-nm) error to the Mueller coefficients via the analysis arm.

We can combine the errors from the transmitter and receiver by multiplying the signal-plus-error from the transmitter to the signal-plus-error of the receiver and then removing the signal. For example, the 532-nm channel would perform $(1.0109 \quad 1.0048) - 1 = 0.0158$. This method gives us 1.58% (532-nm channel) and 2.17% (1064-nm channel). For a Mueller matrix reported as normalized to its m_{00} value, this results in a maximum Mueller coefficient error of 0.016 and 0.022 for the respective channels.

2.3 Automation and Measurement Rate

Although the DMPL testbed will be used generally on contrived scenes that are likely to remain static or homogeneous for extended times, some environmental effects of interest may change on a time scale of minutes. Therefore, we had a goal of acquiring a full set of 16 measurements within a few minutes. Using the less optimal states for the nonranging polarimeter we built previously,[33] an experienced operator could run the system in 1 to 3 min. However, to improve safety with the higher-power pulsed laser and to narrow our PSG and PSA state tolerances due to repeatable precision for θ_p and θ_f, we implemented motorized rotation stages. The stages reduced the discrete angle tolerance to 0.3 deg, as compared with approximately 1 deg for manual rotation; referring to calculations made in the previous section, the larger tolerance would have resulted in uncertainty propagation of ~1.19× and 1.18× higher than the ideal (κ of 2.06 and 2.04) for the 532- and 1064-nm channels, respectively. These rotation stages are limited in their rotation speed and how many stages can be operated at one time by the software controls.

Even when collecting multiple pulses, the rotation speed of the motorized stages is the limiting factor for measurement rate. Therefore, the order of PSG-PSA state combinations was optimized for minimum total rotation time by determining the total rotation time for each permutation of states and selecting one of the few options with the lowest result. The full set of measurements currently takes just under 3 min regardless of operator experience and with higher polarimetric accuracy than the nonranging polarimeter.

2.4 Variable Scene Distances

The DMPL system is meant to function both in a laboratory environment and outdoors, with scene distances from a few meters up to a few hundred meters. The geometric overlap function of the illumination area and the receiver field-of-view (FOV) depends strongly on the range for all bistatic systems. At long distances, usually more than 100 m, the best overlap is achieved when the optical axes of the Tx and Rx are parallel; however, at shorter distances, the overlap is often zero unless the optical axes are made to cross. When the optical axes cross, maximum overlap occurs in a window around the fixed range where they intersect, falling off at ranges nearer or farther from the lidar. Determining this "weighted" depth of field (the region of full overlap and the edges where partial overlap occurs) requires us to know both the system's Tx divergence and Rx FOV. We determined the Tx divergence by measuring the beam diameter at 3 ranges and fitting those diameters to the equation $D(R) = D_0 + 2R\sin(\theta_{div})$, where D is the beam diameter, D_0 is the initial beam diameter at the transmitter output, R is the range, and θ_{div} is the divergence angle. We determined the Rx FOV half angle, θ_{hFOV}, by scanning a source cross-range at a known range from the receiver input to find the cross-range distances where the signal flattened out; basic trigonometry on the range and these cross-range distances gave us θ_{hFOV}. Using these methods, we found $\theta_{div} = 5.0$ mrad (0.29 deg) and $\theta_{hFOV} \approx 15$ mrad (0.86 deg).

To achieve effective ranging at highly variable scene distances, the receiver was mounted on a rigid optical breadboard and mounted on a locking rotation stage. This allows manual alignment via return maximization from a reference target at a desired scene distance prior to measurements. Retractable legs allow the receiver platform to be leveled and better stabilized once its pointing angle is set. The angle between the Tx and Rx optical axes is referred to herein as the separation angle, ψ. For an optimized scene range of ~2 m, our set up in the optics lab, we find ψ to be ~3.7 deg and a depth of field of ~0.35 m FWHM. For an optimized scene range of ~11.5 m in our lab's laser tunnel, we find $\psi \approx 0.65$ deg and a depth of field of ~10 m FWHM.

3 Calibration and Validation

As an intended reference testbed, we calibrated and validated the DMPL system's responses. The calibration focused on scene reflectance, and we validated the polarimetric measurements against samples with known Mueller responses. In addition, the tolerance on the system's coordinate plane was determined using a polarimetric validation sample.

3.1 Reflectance Calibration

The relative calibration function for our system takes the form of $K(\omega_i, \omega_v)$, with units $(\mathrm{sr} \cdot \mathrm{V} \cdot \mathrm{m}^2)^{-1}$, in the equation relating bidirectional reflectance distribution function (BRDF), f_r, and the range-normalized APD electrical response, $V^R(\omega_v)$

$$f_r(\omega_i, \omega_v) = V^R(\omega_v) \frac{C(\omega_i, \omega_v)}{T_{\mathrm{sys}} \Delta E_0 \cos(\theta_i)} = V^R(\omega_v) K(\omega_i, \omega_v) = R^2 V(\omega_v) K(\omega_i, \omega_v), \quad (3)$$

therefore,

$$K(\omega_i, \omega_v) = \frac{f_r(\omega_i, \omega_v)}{V^R(\omega_v)} = \frac{C_2}{\cos(\theta_i)}, \quad (4)$$

where V is the electrical signal (voltage in our case, though it could just as easily be the current or digital number), R is the range to the reflector, C is the calibration function capturing responsivity and the like, T_{sys} is the transmittance of the receiver system, ΔE_0 is the transmitter irradiance at normal incidence on the sample, C_2 is a constant capturing those three values for operation in set conditions, and ω_i and ω_v are angle vectors (θ, ϕ) for the incidence and viewing directions, respectively. To keep the detector operating within its linear response region across a wide range of sample reflectances, we must also apply different neutral spectral density (ND) filters; for a more reflective sample, we add more ND filters and reduce the total optical power falling on the detectors. Adding ND filters to the system reduces the value of T_{sys} as a multiplier, so generating calibration functions with a T_{sys} modifier, T_{ND}, should cover use cases with varied sample reflectivities.

We measured isotropic, highly Lambertian reference panels with known constant BRDF, $f_r^L(\rho_{ref})$, at a range of T_{ND} to generate both the K_{532} and K_{1064} relative calibration functions. For these types of reference panel, the isotropic nature reduces the BRDF dependencies to $f_r(\theta_i, \theta_v)$, and similarly, the dependencies of the K functions are reduced. For our system, the viewing angle, θ_v, is defined by a fixed separation angle, ψ, from the incidence or illumination angle, θ_i. Therefore, the final form of the relative calibration function for the DMPL system is

$$K_\lambda(\theta_i, \psi; T_{ND}) = \frac{C_\psi}{T_{ND} \cos(\theta_i)}, \quad (5)$$

where we can determine C_ψ as

$$C_\psi = \frac{f_r^L(\rho_{ref}) T_{ND} \cos(\theta_i)}{V^R(\theta_i, \psi)}. \quad (6)$$

This form of the equation is useful for extrapolating K_λ values for eccentric cases from those found under near-ideal conditions.

Although the Spectralon® used for these measurements is highly diffuse, no real material can be truly Lambertian across all angles, and this material is known to be most Lambertian at incidence or viewing angles near surface normal.[36,37] Therefore, we performed measurements at three angles: normal incidence ($\theta_i = 0$), as close as possible to normal viewing ($\theta_i = \psi$), and halfway between the two (the specular case, $\theta_i = \psi/2$). For long distances, and therefore small ψ, we were generally limited to steps of ~0.5 deg.

Selected data and extrapolated values are shown in Fig. 3, limited to the 532-nm case with only five values of T_{ND} following the format in Eq. (5). Note that the data used to calculate C_ψ are isolated to near-normal incidence, the lines plotted in Fig. 3 are not extrapolations on those data, but the application of the derived relative calibration function, K_λ.

For the DMPL system, the value of $C_{0.65^\circ}$ is 0.01405 $(\mathrm{sr} \cdot \mathrm{mV} \cdot \mathrm{m}^2)^{-1}$ for the 532-nm channel and 0.2814 $(\mathrm{sr} \cdot \mathrm{mV} \cdot \mathrm{m}^2)^{-1}$ for the 1064-nm channel. Note that $T_{ND} = 10^{-OD}$, where OD is the total optical density of the applied ND filters, but the actual OD for a ND filter at a specific wavelength is often different than its nominal OD. For example, the ND filters we have in our lab typically have an order of magnitude difference in their OD at 532- and 1064-nm. Therefore, care

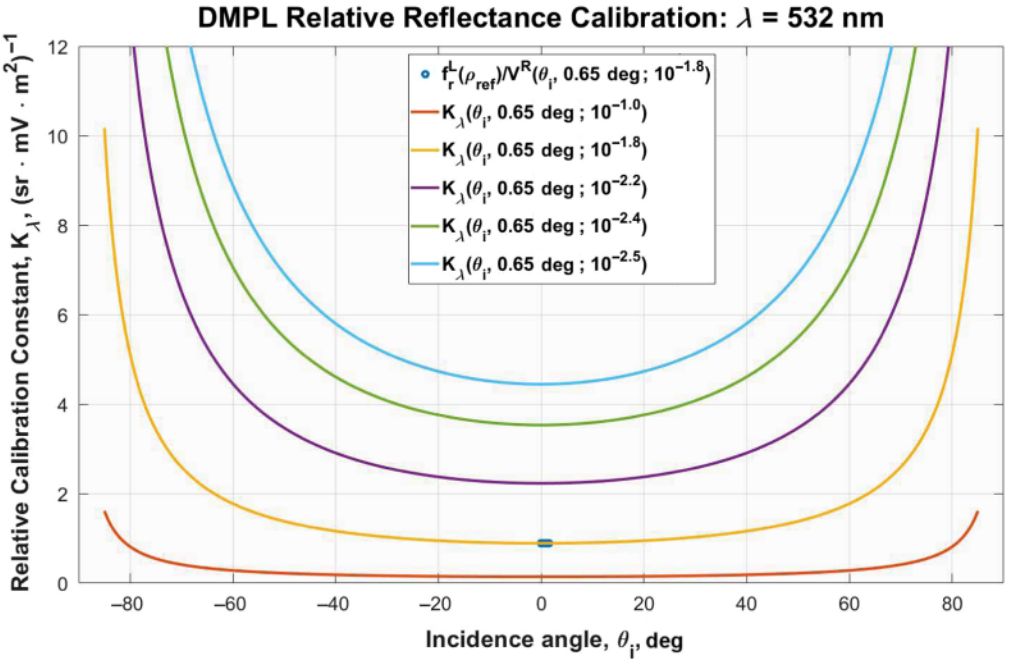


Fig. 3 Plot of K_{532} as a function of θ_i, for a handful of T_{ND} values, as well as the fitted inverse cosine curves extending to values beyond 0 to ψ. These values are for our laser tunnel setup where $\psi \approx 0.65$ deg.

must be taken to apply the appropriate OD values for each wavelength's relative calibration separately, and the most accurate method remains taking calibration measurements with the full intended setup when possible.

3.2 Ranging Validation

For the equipment used, we have a range resolution of ~15 cm (based on the digitizer 1 GS/s sampling rate and confirmed by measurements). Each of the Mueller matrix coefficients above was derived from 16 measurements returned from a single lidar range bin with the sample at a given θ_i. We can also produce figures showing Mueller coefficients as a function of range. This is useful for differentiating multiple staggered or nonopaque samples at different ranges. An example of the Mueller coefficient plots as a function of range is shown in Fig. 4, where we have placed two samples at different range bins such that they are only partially illuminated by the transmitter.

The two cardboard samples were placed in our laser tunnel at ~8.69 and 13.12 m. The lidar returns show peaks in the range bins containing these two values, the first bin from 8.61 to 8.75 m and the second bin from 13.10 to 13.25 m, validating our measured and applied electronic delay. Note that the return is spread over a range of ~1 m at FWHM, which is the appropriate signal distribution for our ~7-ns pulse length. In this and other plots, values for which the signal across the 16 measurements does not rise above the noise threshold are masked out; this prevents the plots from appearing extremely noisy when normalized to the m_{00} coefficient. This plot shows only a signal strength using arbitrary units because the amount of the illumination area falling on each sample in the complex scene cannot be precisely determined. However, for scenes where the illumination area falls entirely on a single sample and that sample's area is under-filled by the illumination, we can use the reflectance relative calibration discussed in Sec. 3.1 to instead report BRDF with units of sr^{-1}.

3.3 Polarimetric Validation

To validate the DMPL as a polarimeter, we measured a diffuse reflector, a scene containing three distinct materials in different range bins, and a specular sample with multiple linear polarizer orientations and a quarter-waveplate (QWP) in front of the receiver.

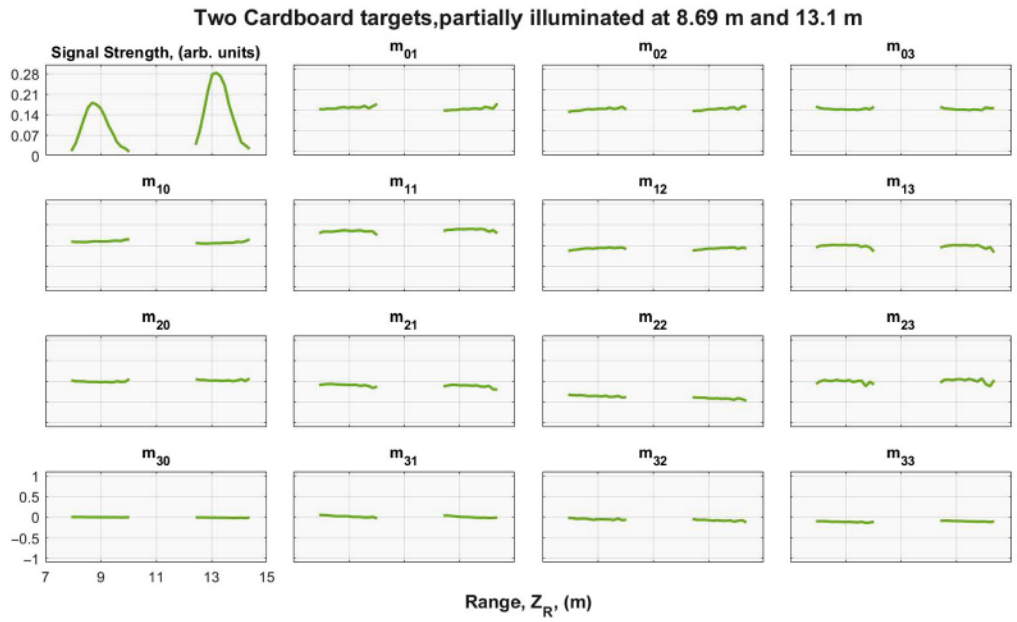


Fig. 4 Plot of Mueller coefficients in the 532-nm channel as a function of range for two cardboard samples at a range of 8.69 and 13.1 m. Note that the Mueller coefficients are normalized to m_{00}, and in place of m_{00}, an arbitrary signal strength is plotted instead. Range values for which the signal is at or below the noise threshold are masked out of the plots. All plots share the same *x*-axis scale and limits, and only the upper-left plot has different *y*-axis scales and limits.

The diffuse sample is expected to be as near a perfect depolarizer as is achievable, represented by all coefficients other than m_{00} having values of 0 (when normalized to m_{00}). The measurements were taken with ND filters totaling OD 1.80 in place and with the entire beam area falling on the 30 cm by 30 cm square panel. The resulting Mueller matrix for the diffuse material for θ_i ranging from −60 deg to 60 deg in 5 deg increments is shown in Fig. 5. The flat, mostly gray response, is the expected result for a highly depolarizing sample such as this. Within the expected error of ∼ 0.02 for the m_{00}-normalized coefficients, this plot shows the expected

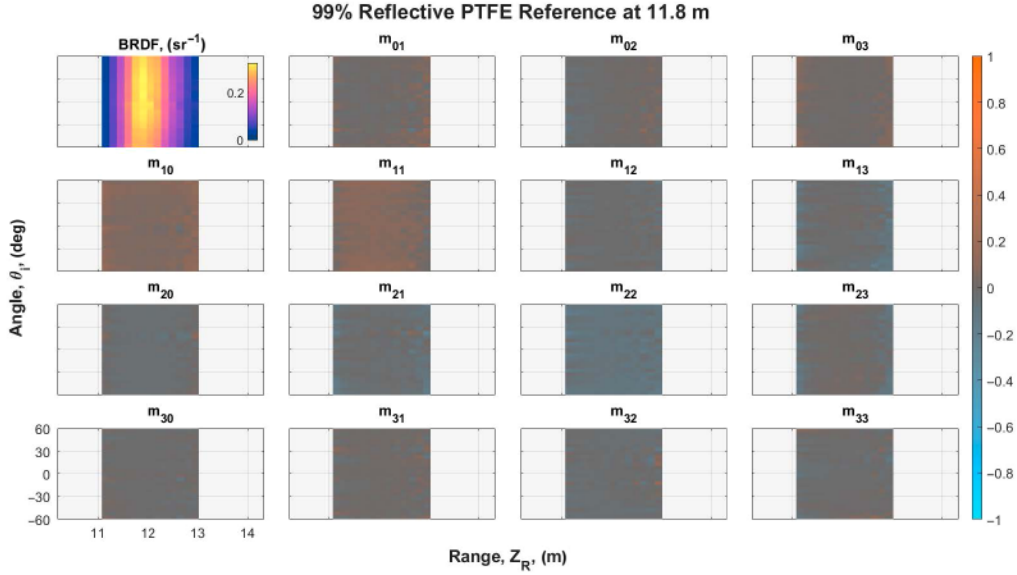


Fig. 5 Plot of Mueller coefficients for a 99% reflective Spectralon® sample from −60 deg to 60 deg in steps of 5 deg. Note that the very small values of the coefficients are 0 to within the system error. No data are shown for range-angle combinations where there was no detectable return signal above the noise. Each plot shares the same *x*- and *y*-axis scale and limits.

polarimetric response from Spectralon® references measured in the previous literature,[32,36–38] and, though a bit harder to quantify by looking at the plot, the cross-range slices of the BRDF plot are flat as expected [given their cosinusoidal correction relative to θ_i based on the K_λ calculation in Eq. (5)].

For a more complex scene, we placed a plant at 8.23 m, a piece of cardboard at 9.75 m, and a piece of aluminum at 11.89 m. The plant was placed so it cast a shadow onto the cardboard, and only a very small sliver of the beam passed the cardboard to the aluminum (otherwise, the return from the metal would be much too bright compared with the other returns). These three materials were chosen to show distinct polarimetric and spectral signatures. The plant and cardboard are relatively diffuse, with the plant being a bit glossier in the visible wavelengths, whereas the aluminum provides a near-specular response, which is partially tempered in the visible by the striations left on its surface from milling. Live plants are commonly known to have higher reflectance in the infrared than the visible, which can be compared with the relatively flat spectral response of diffuse cardboard. Similarly, the milling striations in the aluminum should have less effect at larger wavelengths, so we expect to see a sharper peak signal in the lidar return due to reduced multiple scattering. The processed data for the 532- and 1064-nm channels are shown in Figs. 6 and 7, respectively, and do show all of the expected trends. The plotted data also show appropriate separation between signals based on the pulse width.

The specular sample was measured independently to generate a scene Mueller matrix, $\mathbf{M_{sc}}$, represented as a combination of

$$\mathbf{M_{sc}}(\omega_i, \omega_v) = \mathbf{M_P}(\omega_v)\mathbf{M_{spec}}(\omega_i, \omega_v), \tag{7}$$

where $\mathbf{M_{spec}}$ is the polarized response of the specular sample alone and $\mathbf{M_P}$ is the expected response of the transmissive polarizing element placed in front of the receiver. For small separation angles, ψ, the values of ω_i and ω_v are functionally equal, and constraining sample rotation to the horizontal plane and a fixed position of the polarizer, Eq. (7) reduces to

$$\mathbf{M_{sc}}(\theta_i) = \mathbf{M_P}\mathbf{M_{spec}}(\theta_i). \tag{8}$$

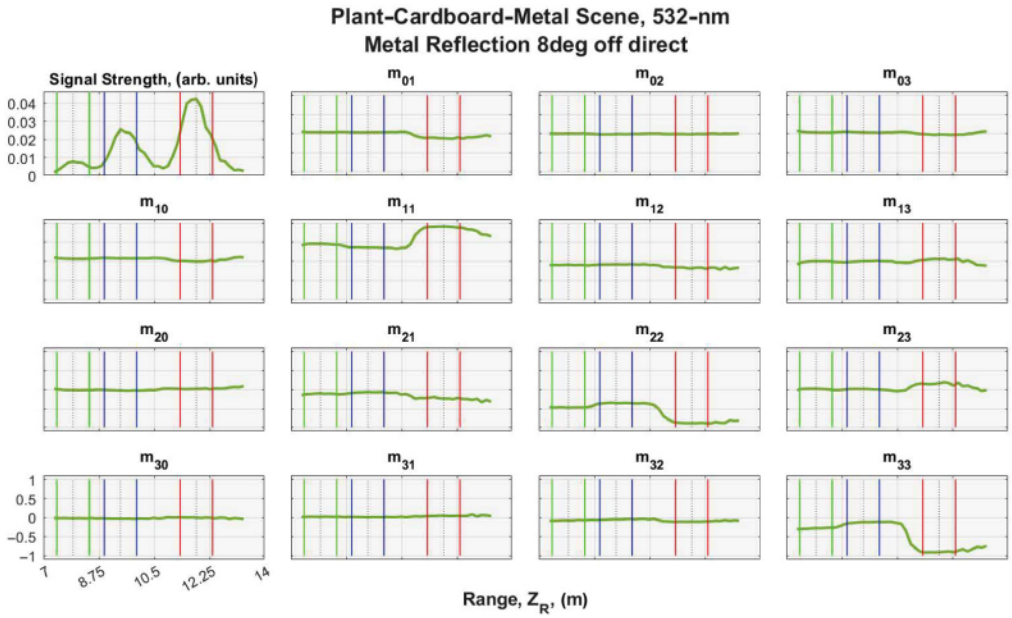


Fig. 6 Plot of Mueller coefficients in the 532-nm channel as a function of range for three partially illuminated samples: a plant at 8.23 m, cardboard at 9.75 m, and aluminum at 11.89 m. The peak signal for each sample is shown with a vertical dotted line, and the unambiguous range resolution around those peaks is denoted with colored vertical lines: green (plant), blue (cardboard), and red (aluminum). Note that the Mueller coefficients are normalized to m_{00}, and in place of m_{00}, an arbitrary signal strength is plotted. All plots share the same x-axis scale and limits, and only the upper-left plot has different y-axis scales and limits.

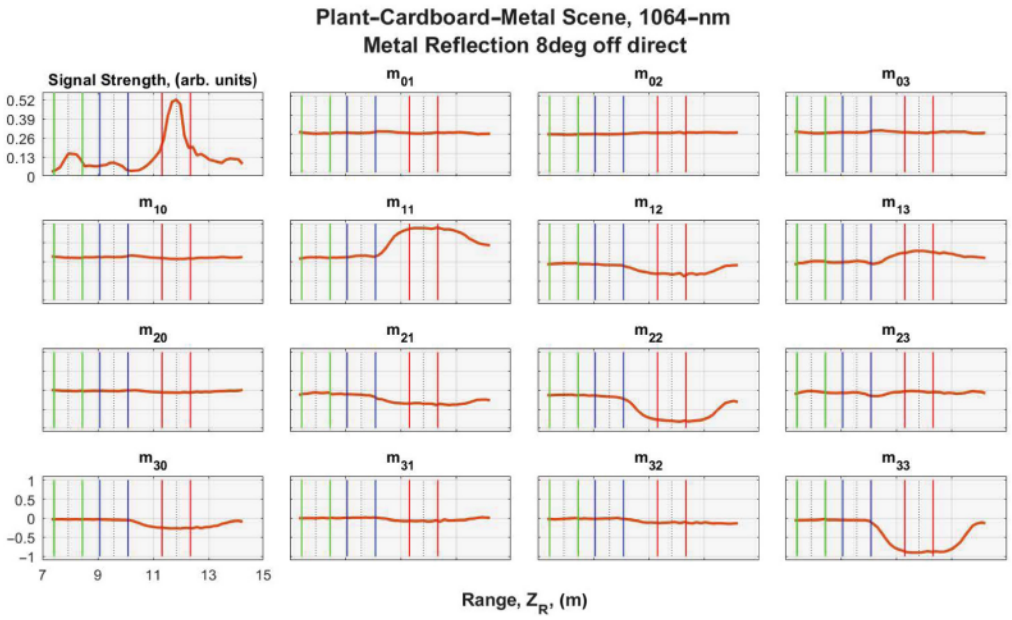


Fig. 7 Plot of Mueller coefficients in the 1064-nm channel as a function of range for three partially illuminated samples: a plant at 8.23 m, cardboard at 9.75 m, and aluminum at 11.89 m. The peak signal for each sample is shown with a vertical dotted line, and the unambiguous range resolution around those peaks is denoted with colored vertical lines: green (plant), blue (cardboard), and red (aluminum). Note that the Mueller coefficients are normalized to m_{00}, and in place of m_{00}, an arbitrary signal strength is plotted. All plots share the same *x*-axis scale and limits, and only the upper-left plot has different *y*-axis scales and limits.

Using standard polarimetric analysis (see the Chipman textbook[35]), the sets of 16 measurements, represented by $\vec{I}$, are multiplied by $\mathbf{W}^{-1}$ to retrieve $\mathbf{M}_{sc}$; $vec(\mathbf{M}_{sc}) = \mathbf{W}^{-1}\vec{I}$.

For the specular measurements, we used a piece of aluminum as the sample, which required OD 3.80 to prevent saturation. At the specular angle, this sample has a Mueller matrix close to an identity matrix but with the m_{22} and m_{33} coefficients having a negative sign (indicating π phase offset). The surface is not as smooth as a high-quality mirror but still serves as a largely non-depolarizing sample. At the sample range of 11.7 m, the aluminum's polarized response at 532 nm was measured as

$$\mathbf{M}_{\mathbf{spec}}^{\mathbf{532}} = \begin{bmatrix} 1.00 & 0.09 & 0.01 & 0.03 \\ 0.09 & 0.95 & 0.28 & -0.03 \\ 0.04 & 0.25 & -0.94 & 0.13 \\ -0.02 & 0.03 & -0.15 & -0.93 \end{bmatrix}. \tag{9}$$

A notable feature of the aluminum sample was a diffraction effect orthogonal to milling striations on the metal surface. For the data presented in Eq. (9), these striations were horizontal, causing diffraction in the vertical direction. This grating-like structure may account for the significant above-zero values of m_{01}, m_{10}, m_{12}, m_{21}, m_{23}, and m_{32}, as it increases nonnormal reflectance polarizance/diattenuation as well as induces variable phase retardance. Although $\mathbf{M}_{\mathbf{spec}}^{\mathbf{532}}$ is sufficient for the polarization element analysis we wanted to perform, for an interested reader, we also include the specular sample's Mueller matrix when the diffracting striations are rotated 90 deg (resulting in horizontal diffraction).

$$\mathbf{M}_{\mathbf{spec,Horz}}^{\mathbf{532}} = \begin{bmatrix} 1.00 & -0.02 & -0.01 & 0.03 \\ -0.00 & 0.95 & -0.16 & 0.02 \\ 0.05 & -0.20 & -0.97 & 0.11 \\ -0.01 & 0.03 & -0.13 & -0.91 \end{bmatrix} \tag{10}$$

With the specular sample's response determined, we added a linear polarizer in front of the receiver such that the entire scene was seen through $\mathbf{M_P}$. The polarizer was oriented horizontally (case H, 0 deg), vertically (case V, 90 deg), diagonally (case D, 45 deg), and at a noncardinal angle (case N, 30 deg), all to within 0.5 deg (the uncertainty of the rotational mount used for the validation polarization elements). We can remove the known $\mathbf{M_{spec}}$ from each of the resulting $\mathbf{M_{sc}}$ for scenes to produce the measured Mueller matrices for the polarizers. For the sake of space, only the 532-nm channel's horizontal orientation matrix, $\mathbf{M}_{\mathbf{P,H}}^{532}$, and noncardinal matrix at 30 deg, $\mathbf{M}_{\mathbf{P,N}}^{532}$, are shown here.

$$\mathbf{M}_{\mathbf{P,H}}^{532} = \begin{bmatrix} 1.00 & 1.01 & 0.05 & 0.07 \\ 1.01 & 1.00 & 0.04 & 0.04 \\ -0.01 & 0.02 & 0.04 & 0.01 \\ 0.01 & -0.03 & 0.01 & 0.04 \end{bmatrix}, \tag{11}$$

$$\mathbf{M}_{\mathbf{P,N}}^{532} = \begin{bmatrix} 1.00 & 0.44 & 0.89 & -0.02 \\ 0.54 & 0.23 & 0.47 & -0.02 \\ 0.83 & 0.37 & 0.76 & -0.00 \\ -0.05 & -0.04 & -0.01 & 0.03 \end{bmatrix}. \tag{12}$$

These Mueller matrices are normalized to their m_{00} coefficients for ease of analysis and error discussion. For the $\mathbf{M}_{\mathbf{P,H}}^{532}$ case, the ideal linear polarizer coefficients are zero except for the upper-left quadrant, where the normalized coefficients should all be 1; this is approximately the case as reported in Eq. (11) to within ~0.05 (with one marginal outlier of 0.07). Given the polarizer pass-axis orientation uncertainty of 0.5 deg, we might expect any of the upper-left nine coefficients other than m_{00} (m_{01}, m_{02}, m_{10}, m_{11}, m_{12}, m_{20}, m_{21}, and m_{22}) to be off by up to 0.87% in magnitude but all about equal to each other and of matching sign for the horizontal case. In addition, by dividing one measurement by another, the error propagates through the calculations again, increasing the maximum possible error from 1.57% for the 532-nm channel by a factor of 3.19 ($\kappa_{532,G}$ $\kappa_{532,A}$) for a new maximum expected error of 5.02% when estimating the $\mathbf{M}_{\mathbf{P}}^{532}$ coefficients. With these caveats in mind, the results presented in Eqs. (11) and (12) are within the expected error tolerances, with the exceptions of $m_{03}^{P,H}$ and $m_{21}^{P,N}$, which display errors ~2% higher than expected.

To get a better sense of error in the fourth row and fourth column terms, we also measured a QWP (532-nm design wavelength) at a non-cardinal angle of −6 deg (case E, for elliptical). The waveplate was aligned to within 1 deg of normal incidence with the considered beam, minimizing off-axis phase errors. The waveplate was inserted in place of the previous linear polarizer.

$$\mathbf{M}_{\mathbf{P,E}}^{532} = \begin{bmatrix} 1.00 & -0.01 & 0.00 & 0.02 \\ 0.00 & 0.99 & -0.18 & 0.27 \\ 0.03 & -0.21 & -0.01 & 0.95 \\ -0.02 & -0.23 & -1.04 & -0.01 \end{bmatrix} \tag{13}$$

The ideal QWP at −6 deg should have a Mueller matrix of

$$\mathbf{M}_{\mathbf{P,E-ideal}}^{532} = \begin{bmatrix} 1.00 & 0.00 & 0.00 & 0.00 \\ 0.00 & 0.96 & -0.20 & 0.21 \\ 0.00 & -0.20 & 0.04 & 0.98 \\ 0.00 & -0.21 & -0.98 & 0.00 \end{bmatrix}. \tag{14}$$

The extended maximum theoretical error of 5.02% from above should still apply, and we see only three terms here above that value, with a maximum observed error of 6.53%. Given the 0.5 deg orientation uncertainty, we might expect up to an additional 1.7% error on the bottom-right coefficients (other than m_{33}), which accounts for the largest error seen here. Across all measurements, 20% have >5.02% error, but only 7% have error beyond what might be expected

given our orientation uncertainties, the highest being 13.62% error. These high error values were consistent for a given coefficient in a given scenario across multiple measurement sets. As it is possible for an unknown Mueller matrix to have multiple possible solutions when poorly constrained, there is a distinct possibility that these higher-than-expected errors arise from the use of milled aluminum as our reflector, which is a rather low-quality mirror.

For the five measurement scenarios, the mean magnitude of the measurement error as compared with the ideal expected polarization element responses is 3.05% (case H), 2.63% (case V), 2.68% (case D), 3.04% (case N), and 2.38% (case E). If we take into account the compounded influence of κ when dividing out $\mathbf{M}_{\mathbf{spec}}$ from $\mathbf{M}_{\mathbf{sc}}$, the scene measurement error magnitudes have a maximum observed error of 4.27%, and the mean errors reduce further to 0.96% (case H), 0.82% (case V), 0.84% (case D), 0.95% (case N), and 0.75% (case E). Additional validation with higher-quality, large-area mirrors can be performed in future work using the same procedure before the device is deployed for a given application to potentially cull the handful of observed errors that were above the theoretical expectations.

3.4 Global Rotation Tolerance

The effect of combined offsets of the polarization elements in the PSG and PSA is discussed in Sec. 2.2, but for the many cases where the sample is not mounted to the same level surface as the DMPL, it is important to note the potential coordinate system error. The coordinate system of the DMPL associates horizontal and vertical polarization with the surface on which it is mounted. This was accomplished using a reference polarizer leveled to the smooth optical table's polarized reflection, resulting in an orientation known to within ± 0.5 deg. We used this reference polarizer to determine the orientation of the polarization axis or crystal axes of each of the PSG and PSA polarization elements, with their rotation stage tolerance of ± 0.1 deg. The actual combined tolerance for each type of polarization element is difficult to calculate, but as the combined error is always a geometric sum, it cannot be greater than the simple sum of the errors. Therefore, when measuring a sample at range, DMPL reports cross-range orientation angles relative to the surface it is mounted on with a tolerance not $> \pm 0.6$ deg.

4 Discussion and Conclusion

We have described the design, build, and specifications of a dichroic Mueller pulsed lidar testbed. This testbed device was built with the primary purpose of providing proof-of-concept measurements for more complex polarimetric ranging devices, emphasizing high polarimetric accuracy and precision and adaptability to varied control scene scenarios. The instrument is based on a widely accepted dual-rotating-retarder polarimeter architecture in a novel application of a ranging polarimetric lidar system with a well-characterized uncertainty bounded by polarimeter design theory and validated with experimental measurements. The theory and design decisions presented here can be used to build a similar system for these purposes at alternate operating wavelengths or size, weight, and power (SWaP) requirements.

The system was calibrated relative to a Lambertian reflectance standard, so its data could be presented in BRF values. We also validated the system operation relative to the calculated maximum Mueller coefficient tolerances, $\pm 1.46\%$ for the 532-nm channel and $\pm 2.04\%$ for the 1064-nm channel, relative to the expected m_{00} coefficient. The DMPL ranging capability was also validated to be within its range-bin limit. Inherent coordinate system tolerances were also reported.

This system is currently planned for use in multistatic polarimetry proofs of concept, material discrimination measurements, and early measurements of snow and smoke's volumetric effects on polarized scattering for ranging applications. The entire system fits on a relatively small computer cart to move easily between indoor and outdoor measurement scenes and can be transported to alternate sites by operators with limited training.

Disclosures

The authors declare that there are no financial interests, commercial affiliations, or other potential conflicts of interest that could have influenced the objectivity of this research or the writing of this paper.

Code and Data Availability

The data underlying the results presented in this paper are not publicly available at this time but may be obtained from the authors upon reasonable request.

Acknowledgments

This material (AFRL-2025-0981) is based on research sponsored by the Air Force Research Laboratory directly under agreement number FA8650-21-1-1176. The U.S. Government is authorized to reproduce and distribute reprints for Governmental purposes, notwithstanding any copyright notation therein. The views and conclusions contained herein are those of the authors and should not be interpreted as necessarily representing the official policies or endorsements, either expressed or implied, of Air Force Research Lab or the U.S. Government.

References

1. S. R. Pal and A. I. Carswell, "Polarization properties of lidar backscattering from clouds," *Appl. Opt.* **12**, 1530–1535 (1973).
2. K. Sassen, "Laser depolarisation 'bright band' from melting snowflakes," *Nature* **255**(5506), 316–318 (1975).
3. K. Sassen, "Polarization diversity LiDAR returns from Virga and precipitation: anomalies and the bright band analogy," *J. Appl. Meteorol. Climatol.* **15**(3), 292–300 (1976).
4. K. Sassen, "Ice crystal habit discrimination with the optical backscatter depolarization technique," *J. Appl. Meteorol. Climatol.* **16**(4), 425–431 (1977).
5. J. D. Houston and A. I. Carswell, "Four-component polarization measurement of lidar atmospheric scattering," *Appl. Opt.* **17**, 614–620 (1978).
6. M. Floc'h et al., "Polarimetric considerations to optimize lidar detection of immersed targets," *Pure Appl. Opt.: J. Eur. Opt. Soc. Part A* **7**, 1327 (1998).
7. S. Tan, J. Stoker, and S. Greenlee, "Detection of foliage-obscured vehicle using a multiwavelength polarimetric lidar," in *IEEE Int. Geosci. and Remote Sens. Symp.*, pp. 2503–2506 (2007).
8. M. R. Roddewig et al., "Dual-polarization airborne lidar for freshwater fisheries management and research," *Opt. Eng.* **56**(3), 031221 (2017).
9. M. R. Roddewig et al., "Airborne lidar detection and mapping of invasive lake trout in yellowstone lake," *Appl. Opt.* **57**, 4111–4116 (2018).
10. G. G. Gimmestad, "Reexamination of depolarization in lidar measurements," *Appl. Opt.* **47**, 3795–3802 (2008).
11. M. Hayman and J. P. Thayer, "General description of polarization in lidar using Stokes vectors and polar decomposition of Mueller matrices," *J. Opt. Soc. Amer. A* **29**, 400–409 (2012).
12. J. M. Richardson, J. C. Aldridge, and A. B. Milstein, "Polarimetric lidar signatures for remote detection of biological warfare agents," *Proc. SPIE* **6972**, 69720E (2008).
13. G. A. Roy, X. Cao, and R. Bernier, "On linear and circular depolarization LIDAR signatures in remote sensing of bioaerosols: experimental validation of the Mueller matrix for randomly oriented particles," *Opt. Eng.* **50**(12), 126001 (2011).
14. C. Keyser et al., "Single-pulse Mueller matrix polarimeter for rapid scene characterization LADAR," *Proc. SPIE* **10655**, 106550G (2018).
15. C. K. Keyser et al., "Single-pulse Mueller matrix lidar polarimeter: modeling and demonstration," *IEEE Trans. Geosci. Remote Sens.* **57**(6), 3296–3307 (2019).
16. J. Brown et al., "Polarimetric lidar feature selection for material classification," in *IEEE Res. and Appl. of Photonics in Defense Conf. (RAPID)*, pp. 1–3 (2020).
17. R. K. Martin et al., "Pixel material classification using polarimetric lidar active imaging," *Appl. Opt.* **64**(18), E53–E61 (2025).
18. D. H. Goldstein and R. A. Chipman, "Error analysis of a Mueller matrix polarimeter," *J. Opt. Soc. Amer. A* **7**(4), 693–700 (1990).
19. J. S. Tyo, "Considerations in polarimeter design," *Proc. SPIE* **4133**, 65–74 (2000).
20. D. Sabatke et al., "Optimization of retardance for a complete Stokes polarimeter," *Opt. Lett.* **25**(11), 802–804 (2000).
21. J. S. Tyo, "Design of optimal polarimeters: maximization of signal-to-noise ratio and minimization of systematic error," *Appl. Opt.* **41**(4), 619–630 (2002).
22. J. S. Tyo et al., "Review of passive imaging polarimetry for remote sensing applications," *Appl. Opt.* **45**, 5453–5469 (2006).
23. T. Mu et al., "Error analysis of single-snapshot full-stokes division-of-aperture imaging polarimeters," *Opt. Express* **23**(8), 10822–10835 (2015).
24. J. S. Tyo, "Extending optimization to active Mueller polarimeters," *Proc. SPIE* **4819**, 68–74 (2002).

25. J. S. Tyo et al., "Design and optimization of partial Mueller matrix polarimeters," *Appl. Opt.* **49**(12), 2326–2333 (2010).
26. Y. Liang et al., "Analysis of errors in polarimetry using a rotating waveplate," *Appl. Opt.* **58**(36), 9883–9895 (2019).
27. L. Wang et al., "Error analysis and optimization for a full-stokes division-of-space polarimeter," *Appl. Opt.* **62**(25), 6816–6825 (2023).
28. P. A. Williams, A. Rose, and C.-M. Wang, "Rotating-polarizer polarimeter for accurate retardance measurement," *Appl. Opt.* **36**(25), 6466–6472 (1997).
29. J. K. Boger et al., "Error evaluation template for use with imaging spectro-polarimeters," *Proc. SPIE* **5158**, 113–124 (2003).
30. A. De Martino et al., "General methods for optimized design and calibration of Mueller polarimeters," *Thin Solid Films* **455**, 112–119 (2004).
31. E. Compain, S. Poirier, and B. Drevillon, "General and self-consistent method for the calibration of polarization modulators, polarimeters, and Mueller-matrix ellipsometers," *Appl. Opt.* **38**(16), 3490–3502 (1999).
32. N. J. Field, M. R. Roddewig, and J. A. Shaw, "Near-monostatic angular Mueller matrix measurements using a simple laser polarimeter," *Proc. SPIE* **11833**, 118330P (2021).
33. N. J. Field and J. A. Shaw, "Simple near-monostatic Mueller polarimeter," *Appl. Opt.* **63**, 7540–7546 (2024).
34. K. Twietmeyer and R. Chipman, "Optimization of Mueller matrix polarimeters in the presence of error sources," *Opt. Express* **16**(15), 11589–11603 (2008).
35. R. Chipman, W. S. T. Lam, and G. Young, *Polarized Light and Optical Systems*, CRC Press (2018).
36. D. H. Goldstein, D. B. Chenault, and J. L. Pezzaniti, "Polarimetric characterization of Spectralon," *Proc. SPIE* **3754**, 126–136 (1999).
37. N. J. Field et al., "Gray spectralon polarized reflectance deviations from Lambertian," *Proc. SPIE* **12112**, 121120A (2022).
38. T. A. Germer, "Full four-dimensional and reciprocal Mueller matrix bidirectional reflectance distribution function of sintered polytetrafluoroethylene," *Appl. Opt.* **56**(33), 9333–9340 (2017).

Nathaniel J. Field is a PhD candidate at Montana State University. He received his BS degree in electrical engineering, his MS degree in optics, and his PhD in electrical engineering from Montana State University in 2016, 2020, and 2025, respectively. His current research interests include passive and active polarimetry, optical metrology, interferometry, and remote sensing systems for situational awareness applications. He is a member of SPIE.

Joseph A. Shaw is the director of the Optical Technology Center and Distinguished Professor in the Norm Asbjornson College of Engineering at Montana State University in Bozeman, Montana, USA. He develops lidar and imaging systems for environmental remote sensing and teaches classes in remote sensing systems and optical design. He earned his PhD and MS degrees in optical sciences at the University of Arizona, his MS degree in electrical engineering at the University of Utah, and his BS degree in electrical engineering at the University of Alaska Fairbanks. He is a fellow of SPIE and Optica and is the 2019 recipient of the SPIE G. G. Stokes Award.